2014

Length Effects of a Built-in Flapping Flat Plate on the Flow Over a Traveling Wavy Foil

Nansheng Liu

Yan Peng
Old Dominion University, ypeng@odu.edu

Xiyun Lu

Follow this and additional works at: https://digitalcommons.odu.edu/mathstat_fac_pubs

Part of the Fluid Dynamics Commons, Mathematics Commons, and the Statistical, Nonlinear, and Soft Matter Physics Commons

Length effects of a built-in flapping flat plate on the flow over a traveling wavy foil

Nansheng Liu,[1] Yan Peng,[2,*] and Xiyun Lu[1]

[1]*Department of Modern Mechanics, University of Science and Technology of China, Hefei, Anhui 230026, China*

[2]*Department of Mathematics & Statistics and Center for Computational Sciences, Old Dominion University, Norfolk, Virginia 23529, USA*

Flow over the traveling wavy foil with a built-in rigid flapping plate at its trailing edge has been numerically studied using the multi-relaxation-time lattice Boltzmann method and immersed boundary method. The effect of the plate length on the propulsive performance such as the thrust force, energy consumption, and propeller efficiency has been investigated. Three modes (body force dominated, body and tail force competing and tail force dominated modes) have been identified that are associated with different hydrodynamics and flow structures. It is revealed that there exists a better performance plate length region and, within this region, a high propeller efficiency (close to its maximum value) is achieved due to a great increase in propulsive force at a cost of a slight increase in energy consumption. Furthermore, a weak stabilizing effect on locomotion movement is indicated by the slight decrease in the root-mean-square (rms) values of drag and lateral forces.

PACS number(s): 47.15.Tr, 47.11.−j

I. INTRODUCTION

The undulatory locomotion movements of various species of fish are classfied into anguilliform (using large portions of their body during propulsion), subcarangiform (using more than one half wave but less than one full wave on the body), and carangiform (using up to one half wave) modes. Among these modes, the movement of swimming fish generally consists of a laterally undulatory wave traveling from the head to the tail and generating thrust mainly at the tail [1]. Two mechanisms have been proposed to explain how force developed by the lateral muscle is converted to thrust at the tail [2]. The first mechanism is that the body undulations create circular flow patterns that travel posteriorly along with the body wave and ultimately modify the flow around the tail to improve swimming performance [3]. The second mechanism is based on shedding vorticity off the body's trailing edge in the peduncle region, which then modifies the tail flow to increase swimming efficiency [4]. As such, the geometry, morphology, and kinematics of the tail fin are expected to affect the forces exerted on the fluid by a swimming fish and in turn the reaction forces experienced by the body during locomotion [5].

The vast majority of the work to date on fish propulsion has focused on the propulsive function of the body surface, i.e., different kinematics of the body deformation during locomotion and their hydrodynamic effects [6]. Computational fluid dynamic analyses of body movements also provide insights into the role that body deformation plays in the wake flow pattern formation and propulsive force production [4,7,8]. Comparatively little is known about how fish tail fins function during swimming. There are relatively few kinematic data on the movement of the caudal fin during the steady swimming, and even less information on the effect of different tail fin shapes on the wake flow patterns and thrust production [5,9–11]. Among them, Anderson [12] and Wolfgang *et al.* [4] illustrated the generation and manipulation of vorticity in a swimming and turning live fish. Liu *et al.* [13] demonstrated

the vortex shedding from the edges of the body near the tail for the swimming motion of a tadpole. Zhu *et al.* [8] identified the principal mechanisms of vortex control employed in fishlike swimming using the inviscid numerical method in conjunction with experimental data from live fish. Dong *et al.* [14] developed a fully viscous computational model to simulate the force generation and near-body flow field of fish fins, utilizing the experimental data of a bluegill sunfish during steady swimming. It is necessary and important to study the details of the flow structure and wake near a fish and to investigate how the flexibility and shape of the caudal fin modulate the vortex shedding and interaction. In our previous study [15], the effect of flexibility of the fish tail fin on the flow structure and the swimming performance was investigated. We found that when the body undulation is confined to the last of the body length, the thrust becomes larger when the tail fin is stiffer; while the propulsion efficiency remains somewhat unchanged. Therefore, the tail fin shape effects will be studied in this paper.

Although the wakes behind an undulatory swimming fish and the vortical structures are fundamentally three dimensions, two-dimensional studies using a traveling wavy foil are still popular as they provide good relevance in physics to the corresponding three-dimensional problem. For example, Liu *et al.* compared their three-dimensional results [13] with their previous two-dimensional study [16] and revealed the similar hydrodynamic features. The streamlines and the pressure distribution over a large portion of body and tail appear to be two dimensional except within a small region limited to the dorsal and ventral tail [13,17,18]. In particular, the investigation of the swimming performance of fish undulatory motion found that the undulatory motion can reduce three-dimensional effects and the flow has a quasi-two-dimensional property [19]. Therefore, in this study, we focus on the two-dimensional flows, where examining the tail fin shape effects can be reduced to changing the length of the caudal fin. By modeling the stiff tail fin using a rigid flat plate built into the trailing edge point of a traveling wavy foil, we will elucidate the effects of caudal fin size on swimming performance in terms of generating thrust and maintaining steady movement. The wavy foil undergoes a prescribed undulation in the lateral direction to model the swimming fish body while the rigid flat

*Author to whom correspondence should be addressed: ypeng@odu.edu
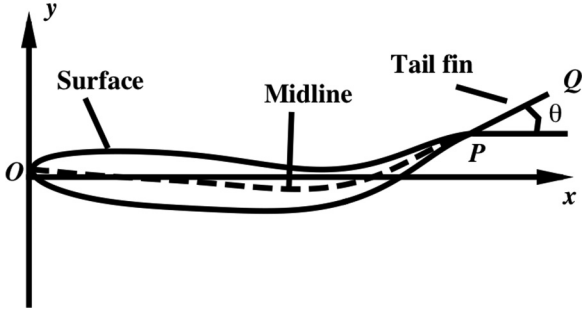
FIG. 1. Sketch of the traveling wavy foil with a rigid flat plate built in at its trailing edge point.

plate takes passively flapping motion to model the caudal fin. Specifically, we want to see whether the length of the tail fin will change the basic mechanisms of the vortex control exerted by the tail fin in order to recover energy or maximize thrust and in turn affect the propulsive performance of the main body.

The remainder of the paper is organized as follows. In Sec. II, the physical problem and the mathematical formulation are described. In Sec. III, we will give a brief introduction to the numerical methods. Detailed results are discussed in Sec. IV. Finally, we conclude the paper with a summary in Sec. V.

II. PHYSICAL PROBLEM AND MATHEMATICAL FORMULATION

As shown in Fig. 1, the viscous flow over a wavy foil body with a rigid flat plate built into its trailing edge is considered. The starting point of the wavy foil is fixed at (0,0) and it undergoes prescribed undulations in the lateral direction. The flat plate to model the stiff tail fin extends out from point P along the tangential direction of the midline. Therefore, the flat plate makes a passively flapping motion with the undulating wavy foil. This is similar to the experiment carried out by Lauder *et al.* [20] that the swimming fish is held behind the head to allow only the imposition of heave and pitch motions. As in the previous experimental, theoretical, and computational studies [6,21], we will assume that the oncoming flow is given at constant velocity U_∞, corresponding to the mean steady inline swimming speed. It is equivalent to the flow induced by an undulating fish that is attached to and towed by a rigid tether that translates the fish in a stagnant fluid at constant velocity U_∞. Observation and calculation [22,23] show that U_∞ varies by less than 2% during steady swimming, so the assumption of constant U_∞ is a good approximation [24]. Some difference occurs in the interpretation of the results for the foil being freely swimming and possibly dragged through the fluid. Although we recognize the possible limitation of this model, we nevertheless feel that the results will be of help in physical understanding of the relevant mechanisms in the flapping-based locomotion of swimming animals [22].

To nondimensionalize the governing equations, the length of the wavy foil L and the free-stream velocity U_∞ are used as the reference length and velocity, respectively. Thus the Reynolds number Re is defined as $\mathrm{Re} = \frac{U_\infty L}{\nu}$, which is fixed at $\mathrm{Re} = 5000$ for all the simulations in this paper. The

nondimensional governing equations are given as

$$\nabla \cdot \boldsymbol{u} = 0, \tag{1}$$

$$\frac{\partial \boldsymbol{u}}{\partial t} + \boldsymbol{u} \cdot \nabla \boldsymbol{u} = -\nabla p + \frac{1}{\mathrm{Re}} \nabla^2 \boldsymbol{u}. \tag{2}$$

A NACA 0012 airfoil is used as the contour of the wavy foil at an equilibrium position of the undulating motion. The midline makes a lateral oscillation in the form of a wave traveling in the streamwise direction and the nondimensional position is described by

$$y(x,t) = A_m(x) \cos\left(2\pi \frac{L}{\lambda}(x - ct)\right), \quad 0 \leqslant x \leqslant 1, \tag{3}$$

where A_m is the amplitude and c is the phase speed.

To model the lateral motion of the backbone undulation during swimming, the amplitude A_m is approximated by a quadratic polynomial [25],

$$A_m(x) = C_0 + C_1 x + C_2 x^2, \tag{4}$$

where the coefficients C_0, C_1, and C_2 are solved from the kinematic data of a steadily swimming saithe [26], which gives $A_m(0) = 0.02$, $A_m(0.2) = 0.01$, and $A_m(1) = 0.10$. Here we assume that the body undulation is a purely lateral compressive motion [13,16]. In the current study, we fix $\frac{L}{\lambda} = 1$, so that Eq. (3) changes to

$$y(x,t) = A_m(x) \cos[2\pi(x - ct)], \quad 0 \leqslant x \leqslant 1. \tag{5}$$

Most fishes using the carangiform or subcarangiform locomotion mode have the tail fins with the length being less than 0.2 when compared with the body length. Specifically, the tail fin length of European sea bass is around 0.098, rainbow trout is 0.094, sand roller is 0.11, troutperch and pirate perch are 0.111, mountain mullet is 0.114, sablefish is 0.096, and lingcod is 0.115 [27,28]. To this end, the dimensionless length of the flat plate varies from 0 (i.e., only wavy foil is considered) to 0.2, in order to examine the resulting effects on the hydrodynamics and propulsive performance.

III. NUMERICAL METHODS

In this study, a multiblock lattice Boltzmann method with immersed boundary method is used. The detailed information can be found in [15]. We will give a brief description here.

A. Lattice Boltzmann equation

The lattice Boltzmann equation (LBE) with multiple-relaxation-time collision model is written as

$$\mathbf{f}(\boldsymbol{x}_j + \boldsymbol{c}\delta_t, t_n + \delta_t) - \mathbf{f}(\boldsymbol{x}_j, t_n)$$
$$= -\mathsf{M}^{-1} \cdot \hat{\mathsf{S}} \cdot \left[\mathbf{m}(\boldsymbol{x}_j, t_n) - \mathbf{m}^{(\mathrm{eq})}(\boldsymbol{x}_j, t_n)\right], \tag{6}$$

where the bold-font symbols denote Q-tuple vectors, and Q is the total number of discrete velocities:

$$\mathbf{f}(\boldsymbol{x}_j + \boldsymbol{c}\delta_t, t_n + \delta_t) = (f_0(\boldsymbol{x}_j, t_n + \delta_t), f_1(\boldsymbol{x}_j + \boldsymbol{c}_1\delta_t, t_n + \delta_t)\dots,$$
$$f_b(\boldsymbol{x}_j + \boldsymbol{c}_b\delta_t, t_n + \delta_t))^\mathsf{T},$$
$$\mathbf{f}(\boldsymbol{x}_j, t_n) = (f_0(\boldsymbol{x}_j, t_n), f_1(\boldsymbol{x}_j, t_n), \dots, f_b(\boldsymbol{x}_j, t_n))^\mathsf{T},$$

$b = (Q - 1)$ is the number of nonzero discrete velocities, and **f**, **m**, and **m**$^{(eq)}$ represent the vectors whose components are the distribution functions, the velocity moments, and the equilibrium moments, respectively. The $Q \times Q$ transform matrix M maps **f** to **m**, i.e.,

$$\mathbf{m} = \mathsf{M} \cdot \mathbf{f}, \quad \mathbf{f} = \mathsf{M}^{-1} \cdot \mathbf{m},$$

and $\hat{\mathsf{S}}$ is a $Q \times Q$ diagonal matrix of the relaxation rates $\{s_i | 0 < s_i < 2\}$, i.e.,

$$\hat{\mathsf{S}} = \mathrm{diag}(s_0, s_1, \ldots, s_b).$$

The nine-velocity model in two dimensions (D2Q9) is used here. Correspondingly the nine moments are

$$\mathbf{m} = (\delta\rho, e, \varepsilon, j_x, q_x, j_y, q_y, p_{xx}, p_{xy})^{\mathsf{T}}. \tag{7}$$

The density fluctuation $\delta\rho$ and the momentum $\boldsymbol{j} := (j_x, j_y)$ are the conserved moments, while the equilibria of the nonconserved moments, e, ε, $\boldsymbol{q} = (q_x, q_y)$, p_{xx}, and p_{xy}, are functions of the conserved ones. With the low Mach number approximation, we use the following equilibria for the nonconserved moments:

$$e^{(eq)} = -2\delta\rho + 3\boldsymbol{j} \cdot \boldsymbol{j}, \quad \varepsilon^{(eq)} = \delta\rho - 3\boldsymbol{j} \cdot \boldsymbol{j}, \tag{8a}$$

$$q_x^{(eq)} = -j_x, \quad q_y^{(eq)} = -j_y, \tag{8b}$$

$$p_{xx}^{(eq)} = j_x^2 - j_y^2, \quad p_{xy}^{(eq)} = j_x j_y. \tag{8c}$$

For the relaxation parameters, s_7 is determined by the shear viscosity $\nu[\nu = \frac{1}{3}(\frac{1}{s_7} - \frac{1}{2})c\delta_x]$ and s_1 by the bulk viscosity $\zeta[\zeta = \frac{1}{6}(\frac{1}{s_1} - \frac{1}{2})c\delta_x]$. It is required that $s_7 = s_8$ and $s_4 = s_6$. The relaxation rates s_0, s_3, and s_5 for the conserved moments ($\delta\rho$, j_x and j_y) have no effect for the model, while the other relaxation rates, s_2 (for ε) and $s_4 = s_6$ (for q_x and q_y), do not affect the hydrodynamics in the lowest order approximation and only affect the small scale behavior of the model. Usually, the values of s_2 and $s_4 = s_6$ are determined by the linear stability analysis. We use $s_2 = 1.54$ and $s_4 = s_6 = 1.9$ in the present study.

B. Immersed boundary method

For the two-dimensional domain Ω containing a one-dimensional closed boundary Γ, the configuration of Γ can be represented in the parametric form of $\boldsymbol{X}(\varsigma, t)$ for $0 \leqslant \varsigma \leqslant 1$, and $\boldsymbol{X}(0, t) = \boldsymbol{X}(N_\varsigma, t)$, where the parameter ς tracks a material point of the boundary. The equation of motion for a Lagrangian point on the boundary is

$$\partial_t \boldsymbol{X}(\varsigma, t) = \boldsymbol{u}(\boldsymbol{X}(\varsigma, t)) = \int_\Omega \boldsymbol{u}(\boldsymbol{x}, t)\delta(\boldsymbol{x} - \boldsymbol{X}(\varsigma, t))d\boldsymbol{x}, \tag{9}$$

where $\boldsymbol{u}(\boldsymbol{X}(\varsigma, t))$ is the velocity of the marker at position $\boldsymbol{X}(\varsigma, t)$. The velocity $\boldsymbol{u}(\boldsymbol{x}, t)$ in Eq. (9) must satisfy the incompressible Navier-Stokes equations:

$$\frac{\partial \boldsymbol{u}}{\partial t} + \boldsymbol{u} \cdot \nabla \boldsymbol{u} = -\nabla p + \frac{1}{Re}\nabla^2 \boldsymbol{u} + \boldsymbol{f}, \tag{10}$$

where the flow velocity $\boldsymbol{u}$, the pressure p, and the body force $\boldsymbol{f}$ evolve on the Eulerian coordinate system $\boldsymbol{x}$. The body force $\boldsymbol{f}$ in Eq. (10) is related to the boundary force $\boldsymbol{F}$ evolved on the Lagrangian coordinate system $\boldsymbol{X}$ defined by the boundary

Γ as the following:

$$\boldsymbol{f}(\boldsymbol{x}, t) = \int_\Gamma \boldsymbol{F}(\varsigma, t)\delta(\boldsymbol{x} - \boldsymbol{X}(\varsigma, t))\, d\varsigma, \tag{11a}$$

$$\boldsymbol{F}(\varsigma, t) = \boldsymbol{F}(\boldsymbol{X}(\varsigma, t), t). \tag{11b}$$

The following smooth approximation of the Dirac δ function in d dimensions is used:

$$\delta_h(\boldsymbol{x}) = \delta_h(x_1)\delta_h(x_2)\cdots\delta_h(x_d), \quad \boldsymbol{x} \in \mathbb{R}^d, \tag{12a}$$

$$\delta_h(x) = \begin{cases} \frac{1}{4h}[1 + \cos(\frac{\pi x}{2h})], & |x| \leqslant 2h, \\ 0, & |x| > 2h. \end{cases} \tag{12b}$$

In this study, the boundary for the fish body is determined by the prescribed undulatory motion rather than solving the coupled fluid-structure interaction problem as developed by Peskin [29,30], and the passively flapping motion of the built-in rigid plate is determined by keeping it aligned with the midline of the wavy foil at the trailing edge point. Thus the body force $\boldsymbol{f}$ is derived by the direct forcing method [31–33].

C. Multiblock technique

We use the multiblock technique proposed by Yu *et al.* [34] and the details of its application to the multi-relaxation-time collision can be found in [35]. The coarse block boundary is in the interior of the fine block and the fine block boundary is in the interior of the coarse block. Velocity, density, and stress are continuous across the block interface. The three-point Lagrangian formulation is used for the temporal interpolation at the interface. In the present study, a five-level grid system is used. The coarsest grid level has the spatial step size of $0.02L$. Because the spatial step size ratio from a coarse grid to a fine grid is 2, the spatial step size on the finest grid is $L/800$. In the context of the multiblock lattice-Boltzmann method, the nondimensional time step size is 0.02 at the coarsest grid level and 1/800 at the finest grid level.

D. Code validation

The validation of our code for the flow over a traveling wavy foil can be found in [15]. In order to verify that the free parameters ($s2 = 1.54$ and $s4 = s6 = 1.9$) in the MRT have weak effects on the obtained fluid dynamics at the resolved small scales, two different mesh sizes (one with the finest grid spacing $L/400$ and the other with $L/1000$) have been used to check the reliability of the computational results obtained using the finest grid spacing $L/800$ in the present study. A typical value of $l = 0.15$ is chosen as the length of the attached flat plate. The drag and lateral forces over one cycle under three different mesh sizes are shown in Figs. 2(a) and 2(b) respectively. From these figures, we can see good agreements for three different sizes, which assure that $s2$, $s4$, and $s6$ have negligible influences on the fluid behavior in the smallest scales resolved in the present calculations.

IV. RESULTS AND DISCUSSIONS

A. Effect of the tail fin length on force and power consumption

First, we investigate the effect of the tail fin length on the time averaged drag force, power needed, and the efficiency of
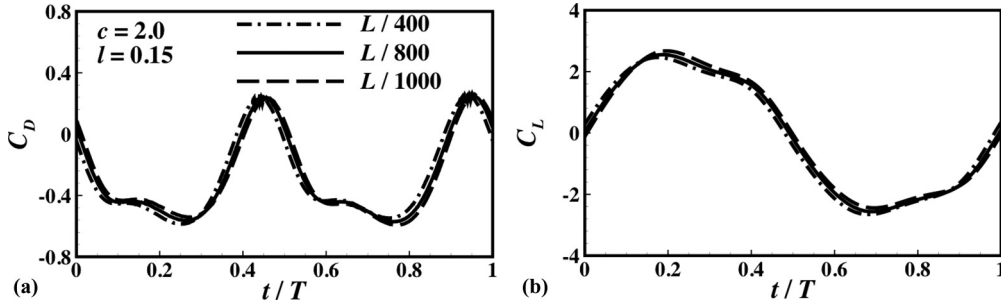
FIG. 2. Comparison of force behaviors for different mesh sizes: (a) drag and (b) lateral forces during one cycle.

the propeller when the net thrust is generated, all of which are fundamentally relevant to the study of fish locomotion. Their definitions are as follows: The total drag force on the fish consists of a friction drag and a form drag due to the pressure distribution. The corresponding drag coefficient is defined as

$$C_D = \frac{F_D}{\frac{1}{2}\rho U_\infty^2 L}. \tag{13}$$

The total power required for the propulsive motion consists of two parts. One part is the swimming power required to produce the lateral oscillation of the traveling wave motion and the movement of the built-in plate, which is defined as

$$P_S = P_{SB} + P_{ST} = -\int_{SB} f_y \frac{dy_w}{dt}ds - \int_{ST} f_y \frac{dy_w}{dt}ds, \tag{14}$$

where SB is the surface of the fish body modeled by the wavy foil, ST is the surface of the tail fin modeled by the flat plate, f_y is the lateral force per unit length on the surface, y_w is the lateral position along the surface, and ds is the length of an element on the surface. The other part is the power needed to overcome the drag force, $P_D = F_D U_\infty = (F_{DB} + F_{DT})U_\infty$, where F_{DB} and F_{DT} are the drag forces coming from the body and tail fin, respectively. Thus the total power is obtained by $P = P_S + P_D$ [36,37]. The propeller efficiency is defined in a time-averaged manner as the ratio of $-\overline{P}_D$ to $\overline{P}_S$, which is $\overline{\eta} = \frac{-\overline{P}_D}{\overline{P}_S}$.

The variations of the time-averaged drag force coefficient, power and the propeller efficiency as functions of the tail fin length are shown in Fig. 3. We can see from Fig. 3(a) that the tail fin length can change not only the force magnitude, but also the sign of the force depending on the value of the phase speed c. The force with positive sign represents the drag

force, while being negative means thrust force. When $c = 1.2$, the drag force is generated and its magnitude decreases slowly with the increase of the tail fin length. For $c = 1.5$, when the tail fin length is less than $l = 0.03$, the drag force is generated. It changes to be the thrust force with longer tail fin and the magnitude increases with the tail fin length considerably. When $c = 2.0$, the propulsive thrust is generated and its magnitude increases with the tail fin length significantly. This is consistent with the previous findings that a fish having a stiff tail prefers high frequency undulatory movement [38].

As we know that the vortical structures are closely associated with the hydrodynamic features, in order to understand why the tail fin length can change the force direction, the vortex sheddings in the wake region for $c = 1.5$ with different tail fin lengths are shown in Fig. 4. To neatly exhibit the flow pattern, only one instant (at $t/T = 1/2$) is given. The jetlike velocity profile in the wake at this instant is also shown in Fig. 5. As we can see from Fig. 4, the shear layer is generated along the body surface and gradually shed into the downstream to form concentrated vortices. When $l = 0$, the wake vortices form an almost in-line vortex street, resulting in the drag force with a magnitude being near zero. When l increases to 0.05, a reverse von Kármán vortex street occurs. This kind of vortical structure induces a jetlike mean velocity profile in the wake, as shown in Fig. 5, which in turn contributes to the thrust generation. Moreover, it is clearly shown that the strength of shedding vortices increases greatly with the increase of the tail fin length and meanwhile the lateral distance between the positive and negative vortices increases due to the larger flapping amplitude with longer tail fins. These two hydrodynamic changes are expected in theory to induce a more intensive jetlike wake flow behind the flapping tail fin. As a result, the decrease in number for the vortex pairs is observed in the wake region. These wake flow pattern modifications are in good agreement
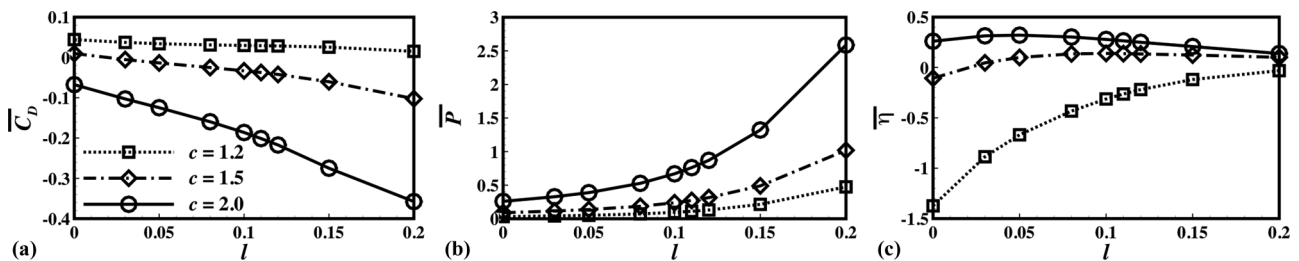
FIG. 3. Variation of (a) the mean drag force coefficient $\overline{C}_D$, (b) the power $\overline{P}$, and (c) the propeller efficiency $\overline{\eta}$ as functions of the tail fin length l.
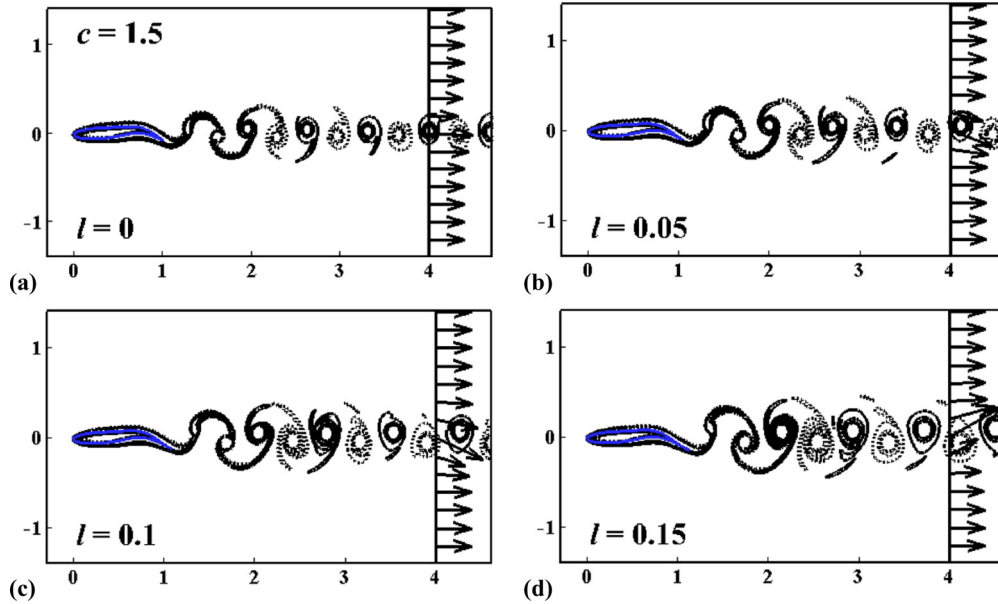
FIG. 4. (Color online) Wake vortex patten for $c = 1.5$, in-line vortex street for (a) $l = 0$ and reverse von Kármán vortex street for (b) $l = 0.05$, (c) 0.1, and (d) 0.15. The vectors in each figure represent the velocity at $x = 4$.

with the recent findings that a von Kármán vortex street forms at a small flapping amplitude, while its transition to an inverse von Kármán vortex street occurs at a certain large flapping amplitude [39].

The power consumption, required for the thrust generation and maintaining the lateral motions of the wavy foil and the flapping plate, exhibits an overall trend of increasing functions of c and l, as shown in Fig. 3(b). Specifically, it is interesting to see that there exists a tail fin length region, from $l = 0.07$ to $l = 0.12$ for $c = 2.0$ for instance, for which a great thrust increase is achieved at an expense of a relatively slight increase in power consumption. When the tail fin is too short (below this region), the thrust increases slightly. However, when the tail fin is too long (above this region), the power consumption increases dramatically. Consequently, as shown in Fig. 3(c), the efficiency takes its maximum value in this region.

To find out why this tail fin length region exists, especially why the power consumption increases remarkably above this region, the propulsive effect of the tail fin length is closely examined by separately evaluating the contributions of the

FIG. 5. Jetlike velocity profile in the wake at $t/T = 1/2$ for $c = 1.5$.

body and tail fin to the hydrodynamic forces. Figure 6 shows the tail fin and body contributions to the mean drag force coefficient, power, and propeller efficiency for $c = 2.0$ as a representative case.

In Fig. 6(a), $\overline{C}_{DT}$ and $\overline{C}_{DB}$ are the mean drag force coefficients calculated for the tail fin and the body contributions, respectively. Based on this figure, we can identify three different modes here. For the small tail fin length ($l \leqslant 0.07$ for $c = 2.0$), the propulsive thrust is mainly generated by the undulatory movement of the body, and we name it as the body force dominated mode. With the middle length ($0.07 < l \leqslant 0.12$), named as the body and tail force competing mode, both the body and the tail fin contribute to the thrust force generation and they play comparable roles. The better performance region happens in the body and tail force competing mode. When the tail fin length is very large ($l > 0.12$), the tail fin contributes most part of the thrust force and we name it as the tail force dominated mode. In particular, in the tail force dominated mode, the drag force can be generated by the body. The reason why the drag force is generated will be explained later by examining the flow field near the body in Sec. IV C. For the power consumption, as shown in Fig. 6(b), the power consumed by the body movement ($\overline{P}_B = \overline{P}_{SB} + \overline{F}_{DB} U_\infty$) does not change too much with the increase of tail fin length, even when the drag force is produced by the body. The power consumed by the tail fin ($\overline{P}_T = \overline{P}_{ST} + \overline{F}_{DT} U_\infty$) behaves differently in three modes. In the body force dominated mode, the power consumed by the tail fin increased slightly. It exhibits a considerable increase in the body and tail competing force mode. When it is in the tail force dominated mode, the power consumption required by the tail fin increases remarkably (with even larger slope). It is expected that the force distribution on the tail fin surface may change greatly in the tail force dominated mode, which will be studied later in this section and in Sec. IV C. As a result of the above-mentioned power consumption feature, the highest efficiency
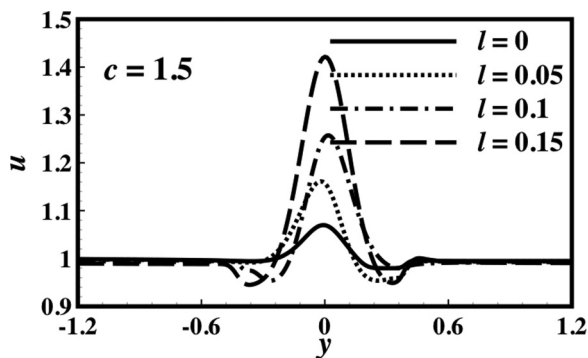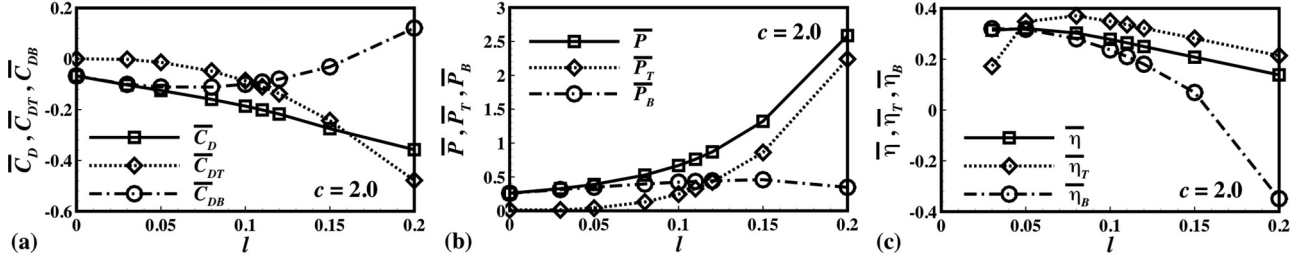
FIG. 6. Tail fin and body contributions to (a) mean drag force coefficient, (b) power, and (c) propeller efficiency for $c = 2.0$.

happens in the body and tail competing force mode as shown in Fig. 6(c). In this figure, the body efficiency ($\overline{\eta}_B$) and tail fin efficiency ($\overline{\eta}_T$) are calculated by $\overline{\eta}_B = -\overline{F}_{DB} U_\infty / \overline{P}_{SB}$ and $\overline{\eta}_T = -\overline{F}_{DT} U_\infty / \overline{P}_{ST}$, respectively.

Second, the effect of the tail fin length on the steady movement is studied by examining the root-mean-square (rms) values of the drag force and the lateral force, which are shown in Fig. 7. The smaller the rms values of drag and lateral forces, the more steadily the fish moves. In the body force dominated mode, the rms values of drag and lateral forces almost stay constant. They vary slightly in the body and tail competing force mode and increase remarkably in the tail force dominated mode. In the better performance region (about from $l = 0.07$ to $l = 0.12$ for $c = 2.0$), introduced when we study the effect of tail fin length on the time averaged parameters, the rms values take the smallest values, which indicates that the fish can propel itself forward efficiently in a more stable manner with lower level oscillations in the forward and lateral movements, namely, a flapping tail fin with its length within this region has a weak stabilizing effect for the fish locomotion movements. Also we can see that when c increases from $c = 1.5$ to $c = 2.0$, the rms value of drag and lateral forces almost double, which may explain the reason why most fishes cruise at the phase speed $c = 1.5$, corresponding to Strouhal number being 0.3 approximately [40].

To elucidate the significant increase for the rms values of force coefficients in the tail force dominated mode, the time-dependent drag and lateral force coefficients in one cycle for $c = 2.0$ are presented in Fig. 8. Meanwhile, since Fig. 6(b) shows that the increase in power consumption mainly comes from the tail fin contribution in the tail force dominated mode, the contributions from the body and tail fin are separately presented in Fig. 9 for further comparison.

Seen from Fig. 8(a), for all the simulations at $c = 2.0$, the drag force coefficient in each cycle shows two peaks. The time

when the thrust force peaks happen demonstrates an evident dependence on the tail fin length in three modes. The thrust force peaks happen at the time around $t/T = 1/2$ and $t/T = 1$ for the body force dominated mode ($l = 0.05$). Further, it can be clearly seen in Fig. 9(a) that the peaks of C_D are in consistency in the occurring time with its body contribution C_{DB}, confirming the body force dominance for the total drag force, which also explains its similarity to the case $l = 0$. We can see later in Sec. IV C the distribution of pressure field results in a large thrust force production at $t/T = 1/2$ and $t/T = 1$ on the body for the body force dominated mode. In contrast, the thrust force peak values happen at around $t/T = 1/4$ and $t/T = 3/4$ for the tail force dominated mode ($l = 0.15$). As the tail fin modeled by a flat plate can be viewed as a very thin flapping foil, this feature is in good agreement with the experimental observations that drag force peaks happen at the forward and backward strokes, which corresponds to $t/T = 1/4$ and $t/T = 3/4$ in our current study. As shown in Fig. 9(e), the peaks of C_D are mainly determined by the peaks from the time-dependent tail fin drag force. For the body and tail competing force mode, $l = 0.1$ here, Fig. 8(a) exhibits two plateaus of the thrust force during one cycle due to the comparable contributions from the body and tail fin shown in Fig. 9(c). In this mode, the drag forces happening in the rigid flapping plate are also suppressed by the movement of the fish body.

The lateral force as shown in Fig. 8(b) also exhibits a large magnitude oscillation during one cycle. Note that the lateral forces in two half strokes are almost equal in magnitude and opposite in direction, thus making negligible contribution to the net lateral force. When we compare the magnitude of the lateral force and drag force, we can clearly see that the lateral force is much larger than the drag force, which agrees with the experimental findings that the majority of locomotor force produced by body is directed laterally by analyzing wake flows in both trout and sunfish [41–44]. In
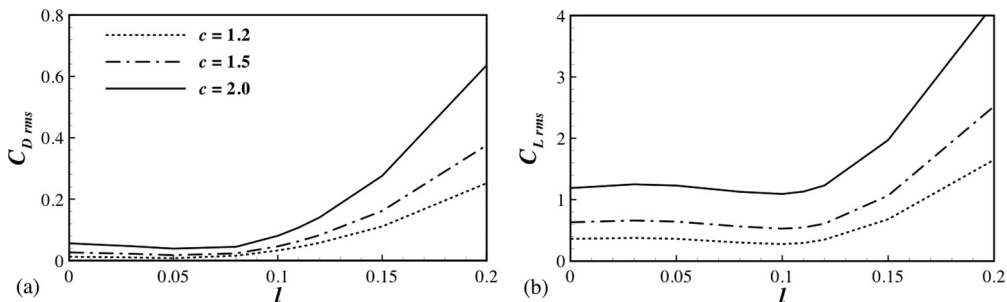
FIG. 7. Root-mean-square values of (a) drag force and (b) lateral force.
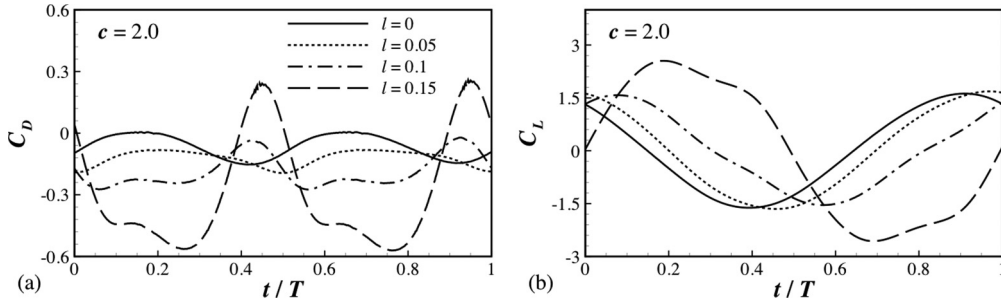
FIG. 8. Time-dependent (a) drag and (b) lateral force coefficients in one cycle for $c = 2.0$.

addition, the current two-dimensional simulations instead of three-dimensional ones also overpredict the lateral force, as reported in the previous work [13]. The dependence of the lateral force on the tail fin length becomes markedly strong only in the tail force dominated mode demonstrated in Fig. 9(f). The magnitude almost doubled when compared with the body dominated and the body and tail competing force modes. Most importantly, in the tail force dominated mode, two wide ranges of phase with large lateral forces are observed, which may explain why the power consumption by the tail fin increases remarkably based on Eq. (14).

Figure 8 also explains that rms values of the drag and lateral forces are small for the body force dominated and body and tail competing force modes. For the tail force dominated mode,

the larger time-averaged thrust is generated at an expense of its higher oscillation with a drag force happening at some certain phases, which is not good for a steady fish swimming in cruise mode. This agrees with the experimental finding that the long tail can act to realize the greatest unsteady motion amplitudes, which would sustain the largest unsteady lifting forces and generate the wake structures with strongest vorticity.

B. Effect of tail fin length on the wake

The vortical wake is closely associated with the hydrodynamic characteristics in fish swimming. So the relation between thrust production and wake vortices is investigated
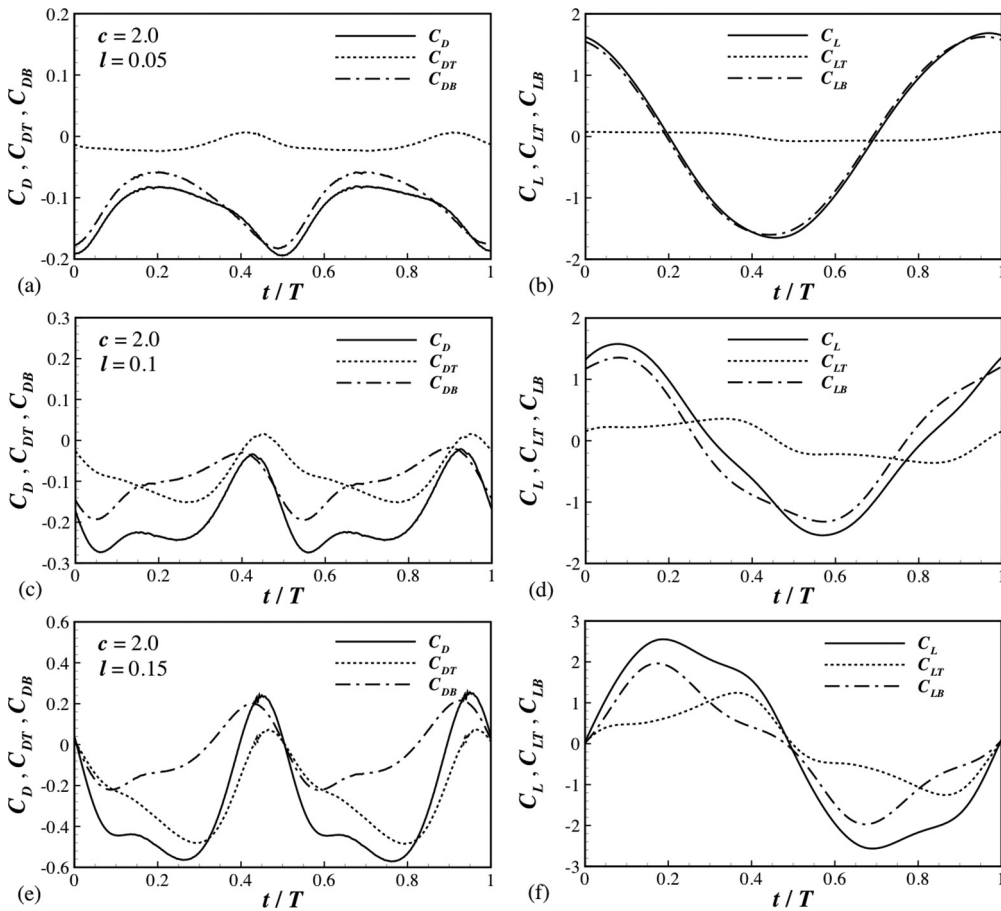
FIG. 9. Contributions of tail fin and body to the time-dependent drag and lateral forces for $c = 2.0$: (a) and (b) are for $l = 0.05$, (c) and (d) are for $l = 0.1$, and (e) and (f) are for $l = 0.15$.
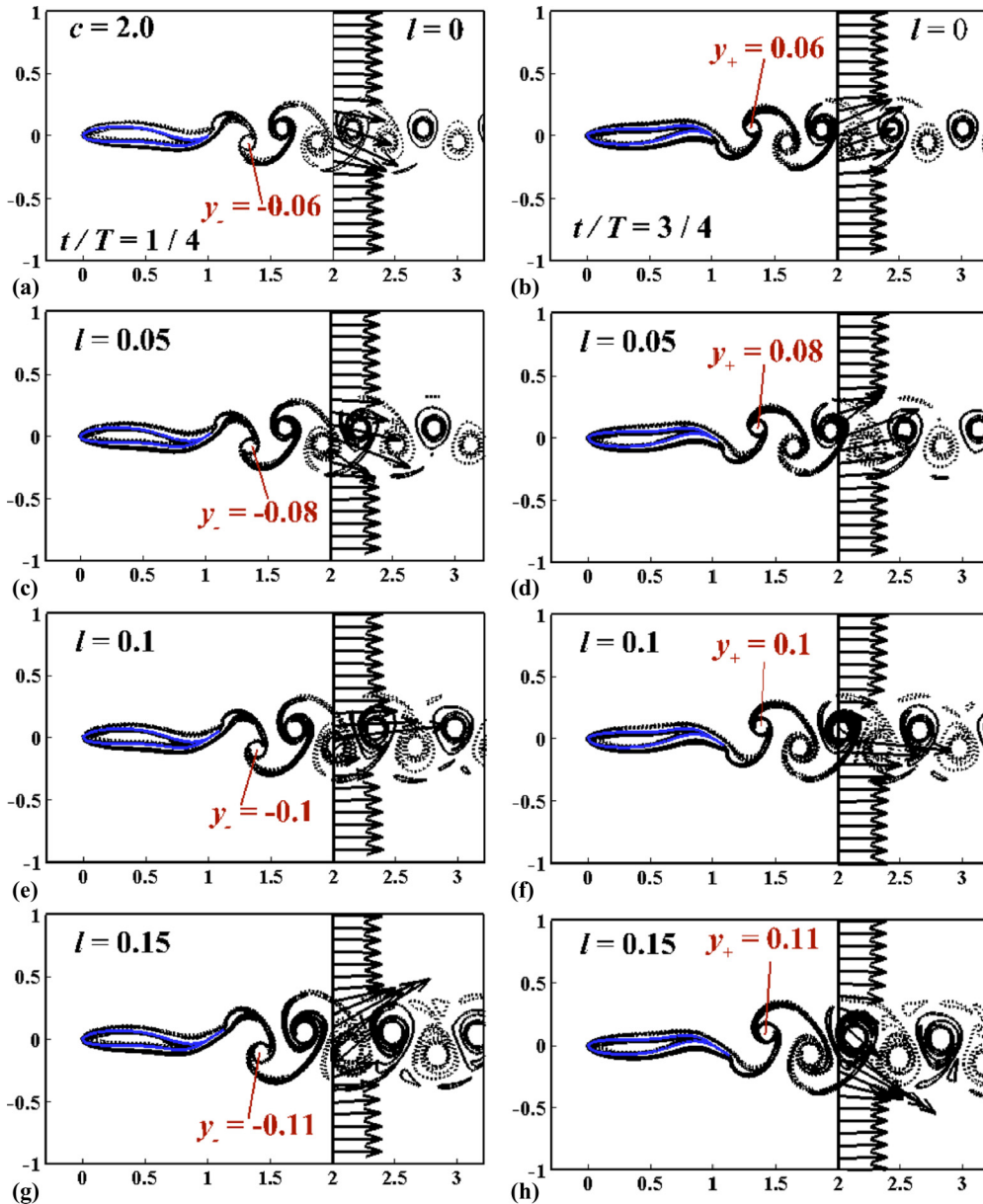
FIG. 10. (Color online) Wake vortex patten at the instants $t/T = 1/4$ and $t/T = 3/4$ for $c = 2.0$: (a) and (b) are for $l = 0$, (c) and (d) are for $l = 0.05$, (e) and (f) are for $l = 0.1$, and (g) and (h) are for $l = 0.15$. In the plots, y_+ and y_- represent the lateral positions of the vortex cores of the first positive and negative shedding vortices in the wake, respectively. The arrows plotted along $x = 2$ denote the velocity vector.

here. The snapshots of vorticity contours at the instants $t/T = 1/4$ and $t/T = 3/4$ for $c = 2.0$ are shown in Fig. 10.

From Fig. 10, for different tail fin lengths, the wake vortices are all arranged in a reverse von Kármán vortex street, in which vortices with positive (negative) intensity are positioned above (below) the horizontal axis ($y = 0$). This vortex arrangement induces a jetlike wake flow on the horizontal axis so that the vortices have a higher downstream advection velocity than the imposed background flow. This jetlike wake flow contributes to the formation of a mean thrust shown in Fig. 3(a) [45]. When the tail fin length increases, vortex shedding occurring at the tip of the tail fin which then has a larger flapping velocity is expected to be delayed. As a result, the wake vortices shed off are advected laterally by higher speed vortical flow causing a larger lateral separating distance between the positive and neg-

ative vortical structures, as well as a decrease in the number of the wake vortical structures in the downstream. In fact, one can see in Fig. 10 that with tail fin length increasing from $l = 0$ to 0.15, the lateral distance of wake vortices increases from 0.12 to 0.22, and meanwhile the number of wake vortices varies from 7 to 6. These modifications of vortex shedding give rise to more intense vortical structures that in turn induce stronger jetlike wake flow, which contributes to larger thrust generation, especially in the tail force dominated mode as demonstrated in Fig. 3(a). The above discussed hydrodynamic effects of delayed vortex shedding on higher thrust generation are similar to the so-called delayed stall mechanism for the high unsteady lift force generation found in the insect hovering flight [46].

Figure 11 shows the corresponding wake flow at $x/L = 2.0$ for different tail fin lengths. With the increase of tail fin length,
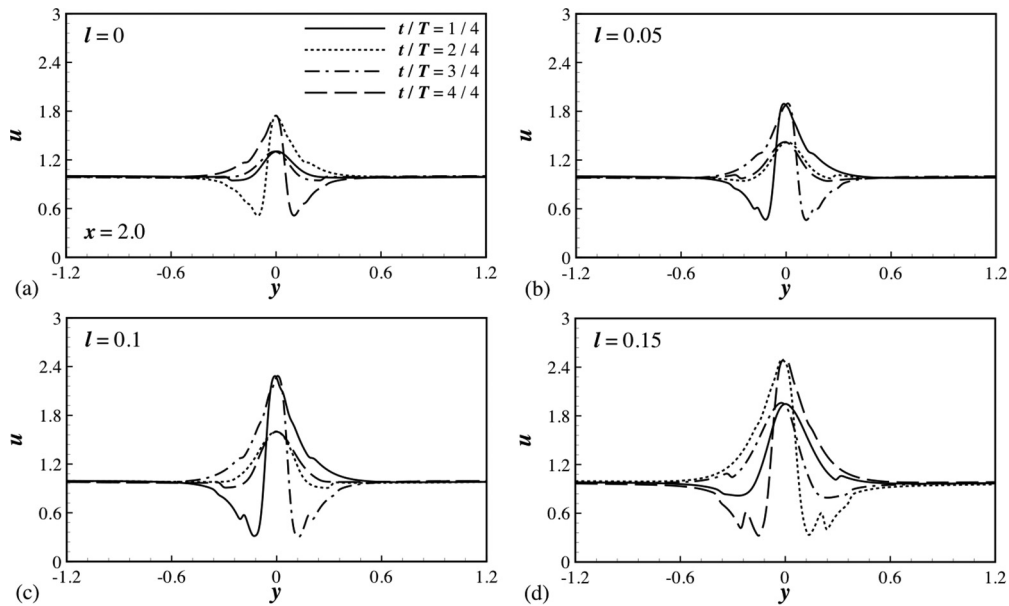
FIG. 11. Jetlike velocity profile in the wake during one cycle for $c = 2.0$: (a) $l = 0$, (b) $l = 0.05$, (c) $l = 0.1$, and (d) $l = 0.15$.

the average magnitude of jetlike velocity increases through different ways depending on the different modes. For the body force dominant mode ($l = 0.05$), the velocity magnitude of the jetlike wake exhibits a slight increase at $t/T = 1/4$ and $t/T = 3/4$, while remaining basically unaltered at $t/T = 2/4$ and $t/T = 4/4$. This is consistent with the behavior of thrust generation at these four instants shown in Fig. 8(a). This may suggest that the body-generated vortices are favorably affected

by the flapping motion of the tail fin [see Fig. 9(a)]. For the body and tail competing force mode ($l = 0.1$) and tail force dominated mode ($l = 0.15$), the magnitude and oscillation of the jetlike velocity increase remarkably. For all the four instances, the regions with momentum surfeits (i.e., the wake flow velocity being greater than the incoming flow) are found to be greater than those with momentum deficits (i.e., wake flow velocity being smaller than the incoming flow velocity),
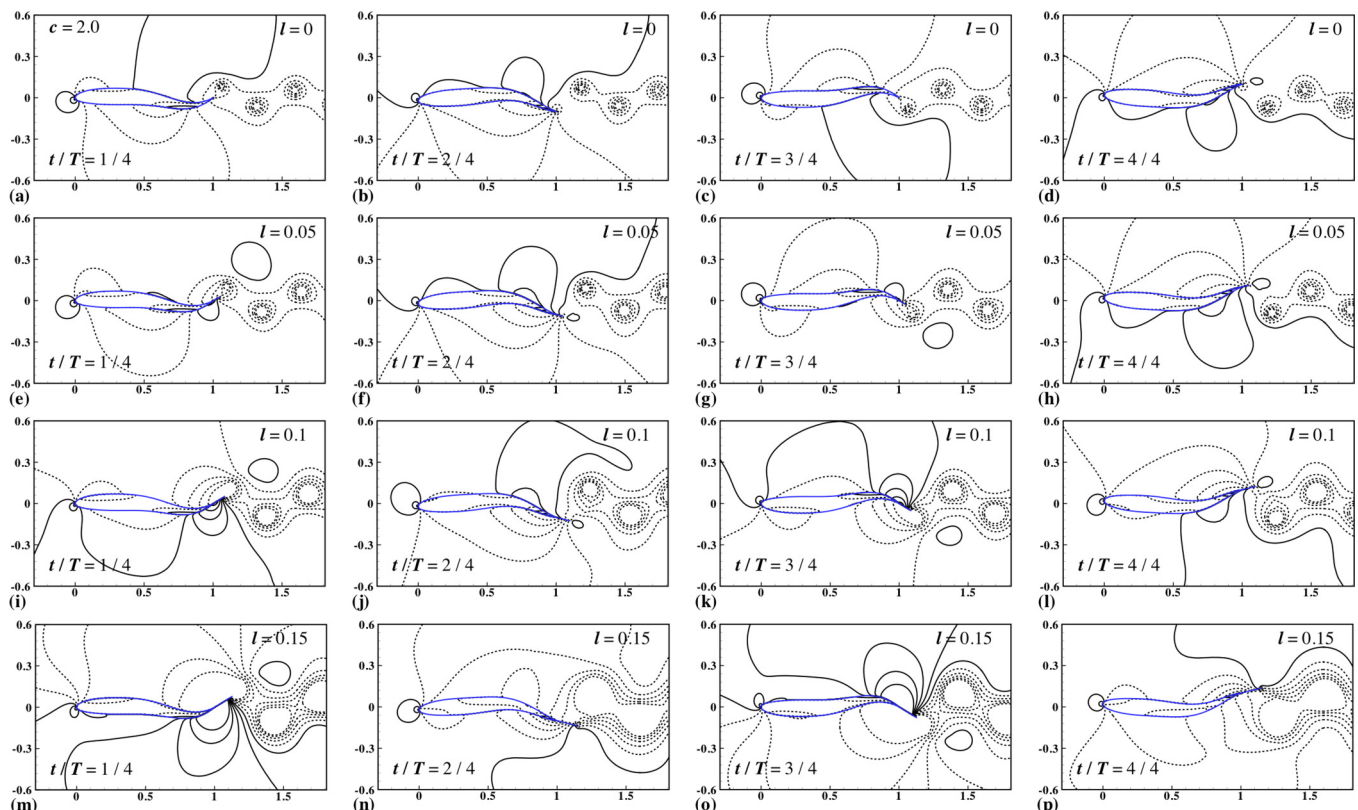
FIG. 12. (Color online) Comparison of the effective pressure contours in the wake for $c = 2.0$: (a)–(d) are for $l = 0$, (e)–(h) are for $l = 0.05$, (i)–(l) are for $l = 0.1$, and (m)–(p) are for $l = 0.15$.
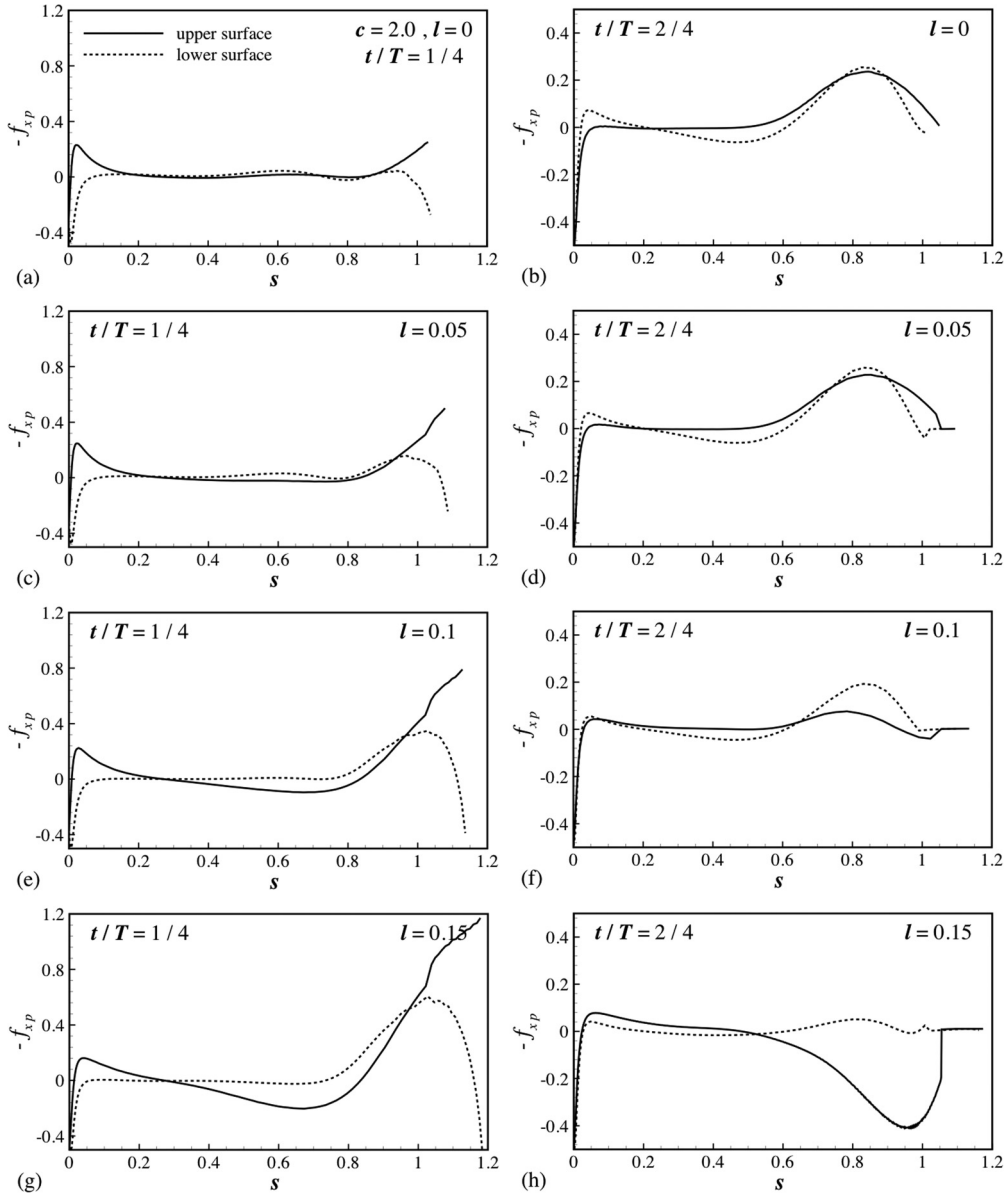
FIG. 13. Distributions of the pressure contribution to the thrust force (i.e., $-f_{xp}$): (a) and (b) are for $l = 0$, (c) and (d) are for $l = 0.05$, (e) and (f) are for $l = 0.1$, and (g) and (h) are for $l = 0.15$.

which agrees with the thrust-producing nature of the wake flow shown in Fig. 10 for $l = 0.1$ and $l = 0.15$. It appears interesting here that although the reverse von Kármán vortex street persists during one full cycle, one can still find in the tail force dominated mode ($l = 0.15$) that small drag force is generated at the unfavorable instances, namely $t/T = 2/4$ and $t/T = 4/4$ for $c = 2.0$, as shown in Fig. 8(a). This result is consistent with the recent observations that the thrust-drag transition does not necessarily occur at the same time as the transition in the wake structure [45,47] or the thrust or wake relation may not be seen as a direct consequence of the wake pattern-induced flow [48].

C. Effect of tail fin length on the pressure field

In this section, we are interested in the origin of the drag force production on the body in the tail force dominated mode. Previous study of the flow over the traveling wavy foil found that the time dependent friction drag force is nearly constant during one cycle, while the thrust force is mainly generated by the favorable surface pressure distribution, i.e., the high-pressure region occurring on the posterior part of the body [49]. Thus, the effective pressure (defined as $p_e = p - p_\infty$) contours at four instants during one cycle for $c = 2.0$ with different tail fin lengths are shown in Fig. 12. To quantitatively show the contribution of pressure distribution to the thrust force, the x-direction component of hydrodynamic force exerted by the surface pressure defined as $f_{xp} = p_e \frac{dy_s}{dx}$ is also presented in Fig. 13 as a function of the surface length s, where y_s is the lateral position of the body or tail fin surface. Due to the fact that the pressure field at antiphases is skew asymmetric about the axis $y = 0$, only the results for $t/T = 1/4$ and $t/T = 2/4$ are presented.

Similar to the findings of the previous study [49], when $l = 0$, the p_e contours reveal low-pressure regions formed on the anterior part, along the contraction region of the fish body. The contribution of pressure distribution on the thrust force mostly occurs over the posterior region of the body, $0.6 < x < 1.0$ at $c = 2.0$. This is clearly demonstrated in Fig. 13(b) with $t/T = 2/4$ when the body generates the largest thrust force. For the body force dominated mode like $l = 0.05$, the pressure field near the body is similar to the pressure distribution for $l = 0$. The actuation of the caudal fin intercepts these low-pressure regions and passes into the region on the inside of the lateral excursion of the caudal fin. As the caudal fin is swept to the other side through the low-pressure region, a reverse Kármán vortex street is formed due to the vortex shedding from the trailing edge of the caudal fin, resulting in the extra thrust force generation on the tail fin shown in Fig. 13(c) with $t/T = 1/4$.

On the contrary, for the tail force dominated mode, like $l = 0.15$ here, the tail fin changes the favorable pressure distribution on the posterior region of the body significantly. Due to the delayed vortex shedding at $t/T = 1/4$, the larger thrust force is generated on the tail fin due to the favorable pressure distribution. When $t/T = 2/4$, since the vortex shedding does not finish, the low-pressure region stays on the upper surface of the body as shown in Fig. 12(n), which leads to the drag force instead of the propulsive force on the upper surface due to the unfavorable pressure distribution as indicated in Fig. 13(h). For the body and tail competing force mode at $l = 0.1$, the surface pressure distribution is determined by both body and tail fin movements, and consequently evident thrust force is generated in both $t/T = 1/4$ and $t/T = 2/4$ as demonstrated in Figs. 13(e) and 13(f).

V. CONCLUSIONS

We have investigated the flow over the traveling wavy foil with a built-in rigid flapping plate attached to its end edge to mimic the stiff fish tail fin. The effects of tail fin length on the force, power consumption, and efficiency are studied. The flow structures near the body and wake are analyzed. Three modes including the body force dominated, the body and tail force competing, and the tail force dominated modes

are identified. A better performance region for the tail fin length is predicted in the body and tail force competing mode. Within this tail fin length region, when compared with the case without a tail fin, the significant increase in the propulsive force is achieved at a cost of slight increase in the energy consumption, which results in a high propeller efficiency near its maximum value; meanwhile a slight decrease in the rms values of drag and lateral forces is found in this region, indicating the weak stabilizing effect of the flapping tail fin. Our numerical finding about the better performance tail fin length region is consistent with the measurements of the tail fin length from some fishes using carangiform or subcarangiform locomotion mode [27,28].

Our study also finds that the tail fin should not be viewed as a simple extension of the body. Rather, the fish tail fin functions as an independent propulsive surface. Flow over the body converges toward the tail, producing a complex flow around the tail fin. The flow field is modified significantly by the presence of the tail fin. Especially, within the body and tail force competing mode, the delayed vortex shedding leads to the great increase in the thrust force and slight change in the lateral force, which is quite similar to the so-called delayed stall mechanism for high lift force generation. This cannot be obtained simply by increasing the amplitude envelope of the body.

Although this study is based on a typical carangiform kinematics matching the experimental curve of Videler [26], the results obtained in this study are helpful to understand the basic mechanisms of the tail fin on the force generation and energy consumption. However, the flow characteristics near the fish is far more complex than the simplified model considered here. Three-dimensional computation around flexible fishlike bodies with a more realistic fin model will be considered in our future work.

[1] M. J. Lighthill, Proc. R. Soc. London B **179**, 125 (1971).

[2] U. K. Müller, J. Smit, E. J. Stamhuis, and J. J. Videler, J. Exp. Biol. **204**, 2751 (2001).

[3] U. K. Müller, B. L. E. Van Den Heuvel, E. J. Stamhuis, and J. J. Videler, J. Exp. Biol. **200**, 2893 (1997).

[4] M. J. Wolfgang, J. M. Anderson, M. A. Grosenbaugh, D. K. P. Yue, and M. S. Triantafyllou, J. Exp. Biol. **202**, 2303 (1999).

[5] G. V. Lauder, Am. Zool. **40**, 101 (2000).

[6] F. Fish and G. V. Lauder, Annu. Rev. Fluid Mech. **38**, 193 (2006).

[7] S. Kern and P. Koumoutsakos, J. Exp. Biol. **209**, 4841 (2006).

[8] Q. Zhu, M. J. Wolfgang, D. K. P. Yue, and M. S. Triantafyllou, J. Fluid Mech. **468**, 1 (2002).

[9] G. V. Lauder and G. A. M. Peter, Exp. Fluids **43**, 641 (2007).

[10] G. V. Lauder, and E. D. Tytell, *Hydrodynamics of Undulatory Propulsion* (Elsevier Academic, Amsterdam, 2006), Vol. 11.

[11] G. J. Li, L. Zhu, and X. Y. Lu, J. Hydrodynamics **24**, 488 (2012).

[12] J. M. Anderson, Ph.D. thesis, Massachusetts Institute of Technology and the Woods Hole Oceanographic Institution, 1996.

[13] H. Liu, R. Wassersug, and K. Kawachi, J. Exp. Biol. **200**, 2807 (1997).

[14] H. Dong, M. Bozkurttas, R. Mittal, P. Madden, and G. V. Lauder, J. Fluid Mech. **645**, 345 (2010).

[15] N. Liu, Y. Peng, Y. Liang, and X. Y. Lu, Phys. Rev. E **85**, 056316 (2012).

[16] H. Liu, R. Wassersug, and K. Kawachi, J. Exp. Biol. **199**, 1245 (1996).

[17] M. S. Triantafyllou and G. S. Triantafyllou, Sci. Am. **272**, 64 (1995).

[18] P. Blondeaux, F. Fornarelli, L. Guglielmini, M. Triantafyllou, and R. Verzicco, Phys. Fluids **17**, 113601 (2005).

[19] J. Cheng, L. Zhuang, and B. Tong, J. Fluid Mech. **232**, 341 (1991).

[20] G. Lauder, J. Lim, R. Shelton, C. Witt, E. Anderson, and J. Tangorra, Marine Tech. Soc. J. **45**, 41 (2011).

[21] M. Triantafyllou, G. Triantafyllou, and D. Yue, Annu. Rev. Fluid Mech. **32**, 33 (2000).

[22] J. J. Videler and F. Hess, J. Exp. Biol. **109**, 209 (1984).

[23] S. Hill, Ph.D. dissertation, University of Leeds, 1998.

[24] T. J. Pedley and S. J. Hill, J. Exp. Biol. **202**, 3431 (1999).

[25] I. Borazjani and F. Sotiropoulos, J. Exp. Biol. **212**, 576 (2009).

[26] J. J. Videler, *Fish Swimming* (Chapman & Hall, London, 1993).

[27] *Grzimek's Animal Life Encyclopedia*, edited by M. Hutchins, D. A. Thoney, P. V. Loiselle, and N. Schlager, 2nd ed. (Gale Group, Farmington Hills, MI, 2003), Vol. 4.

[28] *Grzimek's Animal Life Encyclopedia* (Ref. [27]), Vol. 5.

[29] C. S. Peskin, Ph.D. thesis, Sue Golding Graduate Division of Medical Sciences, Albert Einstein College of Medicine, Yeshiva University, 1972.

[30] C. S. Peskin, Acta Numerica **11**, 479 (2002).

[31] J. Mohd-Yusof, Combined immersed boundaries/B-splines methods for simulations of flows in complex geometries. *Annual Research Briefs*, Center for Turbulence Research, Stanford University, 1997.

[32] Z. Feng and E. Michaelides, J. Comput. Phys. **202**, 20 (2005).

[33] Y. Peng and L. S. Luo, Prog. Comput. Fluid Dyn. **8**, 156 (2008).

[34] D. Z. Yu, R. W. Mei, and W. Shyy, Int. J. Numer. Methods Fluids **39**, 99 (2002).

[35] Y. Peng, C. Shu, Y. T. Chew, X. D. Niu, and X. Y. Lu, J. Comput. Phys. **218**, 460 (2006).

[36] L. Shen, X. Zhang, D. K. P. Yue, and M. S. Triantafyllou, J. Fluid Mech. **484**, 197 (2003).

[37] X. Y. Lu and X. Z. Yin, Acta Mechanica **175**, 197 (2005).

[38] J. R. Nursall, Evolution **12**, 116 (1958).

[39] T. Schnipper, A. Andersen, and T. Bohr, J. Fluid Mech. **633**, 411 (2009).

[40] G. S. Triantafyllou, M. S. Triantafyllou, and M. A. Grosenbaugh, J. Fluids Struct. **7**, 205 (1993).

[41] E. G. Drucker and G. V. Lauder, J. Exp. Biol. **204**, 2943 (2001).

[42] E. G. Drucker and G. V. Lauder, J. Exp. Biol. **208**, 4479 (2005).

[43] E. M. Standen and G. V. Lauder, J. Exp. Biol. **208**, 2753 (2005).

[44] E. M. Standen and G. V. Lauder, J. Exp. Biol. **210**, 325 (2007).

[45] S. Michelin and S. Smith, Phys. Fluids **21**, 071902 (2009).

[46] Y. Liu, N. Liu, and X. Lu, Adv. Appl. Math. Mech. **1**, 481 (2009).

[47] R. Godoy-Diana, J. L. Aider, and J. E. Wesfreid, Phys. Rev. E **77**, 016308 (2008).

[48] V. Raspa, C. Gaubert, and B. Thiria, Europhys. Lett. **97**, 44008 (2012).

[49] G. Dong and X. Y. Lu, Phys. Fluids **19**, 057107 (2007).